applied sciences

MDPI

Article

Enhancing Vibration Isolation Performance by Exploiting Novel Spring-Bar Mechanism

Baiyang Shi [1], Jian Yang [1,*] and Tianyun Li [2,*]

[1] Faculty of Science and Engineering, University of Nottingham Ningbo China, Ningbo 315100, China; baiyang-shi@nottingham.edu.cn
[2] School of Naval Architecture & Ocean Engineering, Huazhong University of Science and Technology, Wuhan 430074, China
* Correspondence: jian.yang@nottingham.edu.cn (J.Y.); ltyz801@hust.edu.cn (T.L.)

Abstract: This study investigates the use of a spring-bar mechanism (SBM) in a vibration suppression system to improve its performance. The SBM, comprising bars and springs, is configured with a conventional linear spring-damper isolator unit. The dynamic response, force transmissibility, and vibration energy flow behaviour are studied to evaluate the vibration suppression performance of the integrated system. It is found that the SBM can introduce hardening, softening stiffness, or double-well potential characteristics to the system. By tuning the SBM parameters, constant negative stiffness is achieved so that the natural frequency of the overall system is reduced for enhanced low-frequency vibration isolation. It is also found that the proposed design yields a wider effective isolation range compared to the conventional spring-damper isolator and a previously proposed isolator with a negative stiffness mechanism. The frequency response relation of the force-excited system is derived using the averaging method and elliptical functions. It is also found that the system can exhibit chaotic motions, for which the associated time-averaged power is found to tend to an asymptotic value as the averaging time increases. It is shown that the time-averaged power flow variables can be used as uniform performance indices of nonlinear vibration isolators exhibiting periodic or chaotic motions. It is shown that the SBM can assist in reducing force transmission and input power, thereby expanding the frequency range of vibration attenuations.

Keywords: spring-bar mechanism; vibration isolation; chaotic motion; power flow analysis; nonlinear stiffness; quasi-zero stiffness

Citation: Shi, B.; Yang, J.; Li, T. Enhancing Vibration Isolation Performance by Exploiting Novel Spring-Bar Mechanism. *Appl. Sci.* **2021**, *11*, 8852. https://doi.org/10.3390/app11198852

Academic Editor: Yves GOURINAT

Received: 4 August 2021
Accepted: 16 September 2021
Published: 23 September 2021

1. Introduction

Scientists and engineers are often confronted with the tasks of preventing the transmission of excessive vibrations from a vibrating source to its surrounding environment [1]. To deal with them, a common approach is to insert a vibration isolator between the source and the receiving structure. For the effective attenuations of the transmitted force (or displacement), the linear vibration isolation theory suggests that the natural frequency of a linear isolator Ω_n has to be much lower than the excitation frequency Ω [2]. As a result, problems can arise when linear isolators are used in harsh environments, such as in cars, ships, aircrafts, and earthquake vibration isolation units, which are subject to shock, impact, or ground motion excitations containing low-frequency components. In these circumstances, successful vibration isolation requires an ultra-low supporting stiffness for a low natural frequency. This, in turn, results in a large static deflection. However, in many practical devices, the maximum allowable deflection is confined, and the use of low static stiffness becomes infeasible. In view of this, many methods have been proposed to improve vibration isolation performance in the low-frequency range without compromising static deflection. One possible approach is to create anti-resonances in the frequency–response curves so that successful isolation is achieved in a relatively narrow band of excitation frequencies [3]. Alternatively, active control units may be introduced to modify the dynamic

characteristics of the isolation system in the low-frequency range, but this approach leads to extra energy costs [4].

Recently, there has been a great deal of interest in configuring passive elements with a linear isolator to achieve low-frequency vibration isolations. These elements, usually referred to as Quasi-Zero-Stiffness (QZS) mechanisms [5] or Negative Stiffness Mechanisms (NSM) [6], can generate a negative restoring force or negative stiffness so that low dynamic stiffness of the overall system is achieved while keeping its static stiffness high and the static deflection small. Such mechanisms are often created by springs [7–10], magnets [11,12], bars [13,14], circular rings [15], or composite plates [16]. By transforming a linear system into a nonlinear system with NSMs, it has been shown that the natural frequency of the linearized system can be reduced. Based on linear vibration theories, the functioning frequency range of these isolation systems will be enlarged, and hence better vibration performance can be expected. Apart from the nonlinear stiffness application in the isolation systems, some researchers have also studied the nonlinear isolation by using electromagnetic shunt damping [17,18]. In recent years, NSMs have also been studied in practical engineering applications and in experimental tests, including drilling systems [19], robots [20], Stewart platforms [21], and vehicle seats [22].

Many previous investigations focused on the displacement response of isolation systems, while the vibration power flow and energy transmission characteristics were often ignored. The vibrational power flow analysis (PFA) combines the effects of both force and velocity responses with a single quantity and can better reflect the transmission of vibration energy within a dynamical system [23]. The power flow analysis approach has been developed into a widely accepted tool to assess vibration transmission in linear/nonlinear dynamical systems [24–27]. Xiong et al. [28] used power flow analysis to investigate the interactional dynamic performance of a system with a vibrating equipment, a nonlinear isolator, and a flexible ship excited by sea waves. Yang et al. studied the power flow behaviour and energy transmission characteristics of the Duffing oscillator [29], a nonlinear absorber [30], and a nonlinear isolator [31]. In recent years, the PFA has also been applied to the coupled oscillators with different nonlinear joints [32–34], with clearance [35,36], or with nonlinear inerter mechanisms [37].

In our previous study [14], a nonlinear isolation system with a NSM created by a pair of bars under constant compression forces was investigated. It was successfully shown that the NSM can reduce the natural frequency of the linearized system and significantly lower the force and power transmission in the low-frequency range. However, it was also found that the NSM is nonlinear and that it can possibly lead to sub-harmonic resonances resulting in a larger response as well as a higher level of power flows at high excitation frequencies. In addition, the NSM introduced softening nonlinearity into the system, thus limiting the maximum allowable deflection to avoid static instability. Therefore, it is necessary to obtain improved NSM design, which can not only assist in low-frequency vibration isolation but can also avoid undesirable nonlinear effects.

To address these issues, this paper develops the previous NSM design by replacing the compression forces with adjustable spring forces dependent on the spring stiffness and the initial deflection. This new configuration based on the spring-bar mechanism (SBM) can better control the stiffness/restoring force characteristics so that effective isolation can be achieved without compromising isolation performance due to nonlinearity. The dynamics and power flow behaviour of the integrated vibration isolation system is investigated thoroughly over the design parameter space so as to make better use of the SBM without introducing undesirable nonlinear effects. In the following content, the SBM and the integrated vibration isolation system model is described. Then, the mathematical model, the stiffness and restoring force characteristics, and bifurcation analysis are presented. The response of the integrated system subject to a harmonic excitation is studied using both analytical approximations based on the averaging method and numerical integrations. Both force transmissibility and power flow characteristics are studied to assess the vibration isolation performance of the system with periodic responses. Moreover, the power flow

characteristics of the system exhibiting possible bifurcations and chaotic responses are examined. Some conclusions are provided at the end of the paper.

2. Mathematical Modelling

2.1. Model Description

As shown in Figure 1a, the current vibration isolation system is developed from a nonlinear isolator model from our previous study, shown in Figure 1b [14]. In both systems, a vibrating mass m is subjected to a harmonic excitation with amplitude f_e and frequency ω. To isolate its vibration from transmitting to base point D, a usual approach is to insert a linear isolator, which comprises a linear vertical spring of stiffness k_1 and a viscous damper with a damping coefficient c. In order to improve vibration isolation performance at low frequencies, a spring-bar mechanism (SBM) can be configured with the linear isolator. Here, the new isolator includes two rigid bars of a fixed length l, with one end pinned together at point E with the mass. Compared to our previous design with a pair of compressed bars [14], there are now horizontal springs with stiffness k_2 connected to the bars so as to enlarge the design space for the stiffness characteristics. The joints A and B can move freely in fixed frictionless horizontal channels. The motion of the system is constrained to the plane of the paper. The static equilibrium position of the mass, at which the bars are horizontal, is taken as the reference position of $x = 0$. Due to the symmetry of the system, the mass m can only have a vertical displacement. In real-world applications, the mass of a force-excited machine is usually much heavier than that of the spring-bar mechanism; therefore, the latter is considered negligible in the current study. It is straightforward to construct the vibration isolator shown in Figure 1a by joining the side walls with the ground wall. In other words, the spring-bar mechanism as well as the vertical mass-spring-damper are configured in a frame. In this way, the experimental prototype of the proposed isolator can be made, and the proposed isolator can be inserted between an applied force and the mounted point, applicable to most engineering scenarios in which vibration isolators are used. Compared to the previous vibration isolator design shown in Figure 1b, which requires the generation of constant compressive force P, the current design in Figure 1a comprising the SBM only requires widely available physical springs and bars and can be realized conveniently in practice.

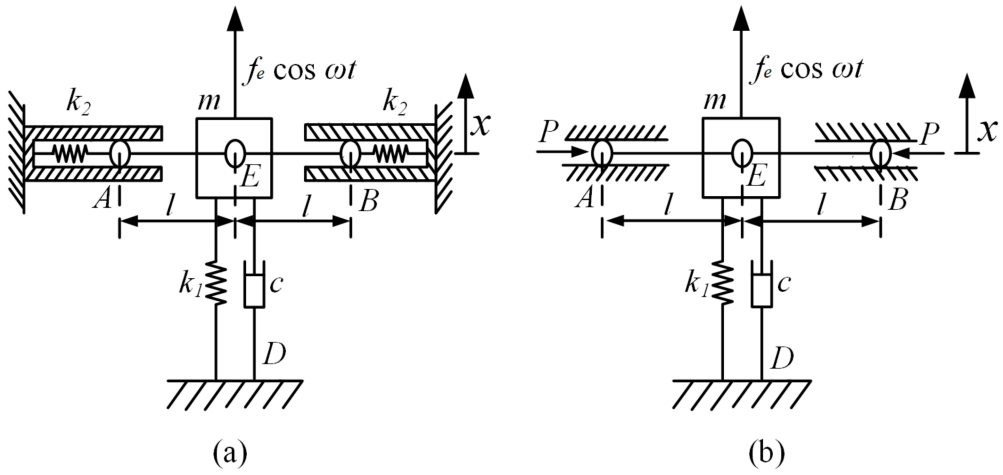

Figure 1. Schematics of the vibration isolation systems with (**a**) the SBM and (**b**) an NSM [14].

Here, we investigate the behaviour of the current SBM alone before studying the dynamics of the integrated system. As shown in Figure 2a, compared to the original length of the horizontal springs, there is an initial deflection of δ_0 when the bars are horizontal. Here, δ_0 is positive when the springs are under tension and negative when under compression. When the bar joint E is subject to a vertical displacement of x, as shown in Figure 2a, the length of each spring increases by $\delta = l(1 - \cos\theta)$, where θ denotes

the angle between the bar $A'E'$ and the horizontal line $A'B'$. Correspondingly, the spring force becomes

$$f_p = k_2(\delta_0 + \delta). \tag{1}$$

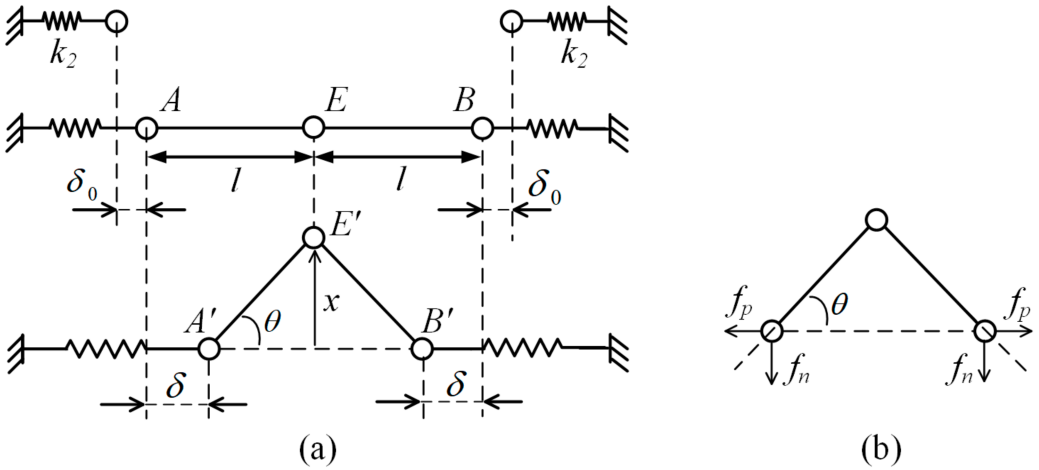

Figure 2. A schematic representation of the SBM system with (**a**) the geometrical deflection and (**b**) a free-body diagram of the bars.

Based on the geometrical relations, we have

$$\sin\theta = \frac{x}{l},\ \cos\theta = \frac{\sqrt{l^2 - x^2}}{l},\ \tan\theta = \frac{x}{\sqrt{l^2 - x^2}}, \tag{2}$$

where $x \neq l$. As the springs and bars are considered to be rigid with negligible mass, the total resultant force applied on the joint E in the vertical direction is

$$f_r = 2f_n = 2f_p \tan\theta, \tag{3}$$

which is also the restoring force of the SBM, as shown in Figure 2b. Using Equations (1) and (3) and replacing the trigonometric terms, we have

$$f_r = 2k_2\left(\delta_0 + l - \sqrt{l^2 - x^2}\right)\frac{x}{\sqrt{l^2 - x^2}} \tag{4}$$

If $\delta_0 = -l$, i.e., the initial compression of the horizontal spring is the same as the length of the bars when x = 0, the restoring force of the SBM will be

$$f_r = -2k_2 x. \tag{5}$$

This equation suggests that the SBM can provide a linear negative restoring force and consequently a constant negative stiffness. By configuring this linear SBM with the vertical spring-damper unit, the dynamic stiffness of the system can be reduced without introducing stiffness nonlinearity.

2.2. Governing Equation

With reference to Equation (4), the governing equation of motion of the vibration isolation system can be written as

$$m\ddot{x} + c\dot{x} + k_1 x + 2k_2\left(\delta_0 + l - \sqrt{l^2 - x^2}\right)\frac{x}{\sqrt{l^2 - x^2}} = f_e\cos\omega t,\ |x| < l. \tag{6}$$

To assist analysis, non-dimensional parameters and variables are introduced as

$$\omega_0 = \sqrt{\frac{k_1}{m}},\ \xi = \frac{c}{2m\omega_0},\ X = \frac{x}{l},\ F_0 = \frac{f_e}{k_1 l},\ \Omega = \frac{\omega}{\omega_0},\ \tau = \omega_0 t,\ \alpha = \frac{\delta_0}{l},\ \beta = \frac{2k_2}{k_1}, \tag{7}$$

where ω_0 is the natural frequency of the linear system without adding the SBM; ξ is non-dimensional damping ratio; X, F, Ω and τ represent the non-dimensional displacement, excitation amplitude, excitation frequency, and time, respectively; α denotes non-

dimensional deflection of the horizontal springs when the bars are in the horizontal direction. Non-dimensional parameter β characterizes the relative stiffness of the horizontal springs against the vertical one and thus can only be positive. Using these parameters and variables, Equation (6) is written into a dimensionless form

$$X'' + 2\xi X' + (1-\beta)X + \beta(1+\alpha)\frac{X}{\sqrt{1-X^2}} = F_0 \cos \Omega\tau, \ |X| < 1 \tag{8}$$

where the primes denote differentiations with respect to the non-dimensional time τ. Equation (8) shows that the SBM introduces a linear term $-\beta X$ in the system and also a possible nonlinear one $\beta(1+\alpha)X/\sqrt{1-X^2}$ when $\alpha \neq -1$. This nonlinearity is affected by different combinations of design parameters α and β. Consequently, for a better application of the SBM, the dynamics of the integrated system should be investigated thoroughly. In comparison, there is only one design variable to control the stiffness in the previous study, and nonlinearity and some undesirable nonlinear phenomena cannot be avoided [14]. Therefore, the current SBM design has a larger degree of control over the dynamic behaviour of the system.

The non-dimensional restoring force of the system is

$$G(X) = (1-\beta)X + \beta(1+\alpha)\frac{X}{\sqrt{1-X^2}}. \tag{9}$$

The overall stiffness of the system is obtained by differentiating $G(X)$ with respect to X:

$$H(X) = (1-\beta) + \frac{\beta(1+\alpha)}{(1-X^2)\sqrt{1-X^2}}. \tag{10}$$

As shown in Figure 3, when $\alpha = -1$, i.e., $\delta_0 = -l$, the restoring force will be proportional to the displacement X, and the system will be linear, with a constant stiffness of $1-\beta$. When $\alpha \neq -1$, the restoring force is a nonlinear function of the displacement, and the system becomes nonlinear. When $(\alpha, \beta) = (-0.5,\ 1.5)$ or $(-0.4,\ 5)$, the stiffness $H(X)$ increases with the deflection $|X|$. For the former case, the stiffness remains positive so that the restoring force increases with X. In comparison, the stiffness of the latter system with $(\alpha, \beta) = (-0.4,\ 5)$ may be negative in the neighbourhood of the static equilibrium position $X = 0$. For a system with $(\alpha, \beta) = (-1.5,\ 0.5)$, it can be seen that the stiffness $H(X)$ decreases with an increasing deflection and that the system exhibits a softening stiffness characteristic. Clearly, the parameters α and β of the SBM should be chosen properly, as they determine the stiffness characteristics of the system.

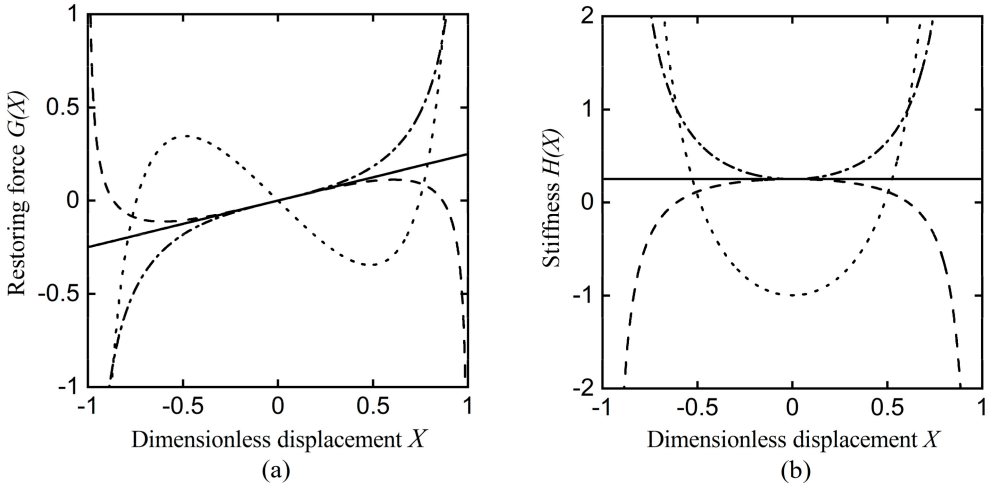

Figure 3. (**a**) Restoring force and (**b**) stiffness characteristics of the system. Solid, dashed, dash–dot, and dotted lines represent systems with $(\alpha,\ \beta) = (-1, 0.75)$, $(-1.5, 0.5)$, $(-0.5, 1.5)$, and $(-0.4, 5)$, respectively.

Using a Taylor expansion of Equation (10) around $X = 0$, the overall stiffness of the corresponding linearized system is found to be $1 + \alpha\beta$. Therefore, for different combinations of α and β with a fixed product, the linearized stiffness at the equilibrium point will be the same. This was demonstrated in Figure 3, in which for three sets of $(\alpha, \beta) = (-1, 0.75)$, $(-1.5, 0.5)$, or $(-0.5, 1.5)$ with $\alpha\beta = -0.75$, the stiffness at $X = 0$ continues to be $H(X) = 0.25$.

The natural frequency of the linearized system is

$$\Omega_n = \sqrt{1 + \alpha\beta}. \tag{11}$$

According to the linear vibration theory, a reduction of the natural frequency leads to a larger effective isolation frequency range. Thus, the value of $\alpha\beta$ can be set close to -1 such that the natural frequency Ω_n tends to zero, yielding a quasi-zero stiffness behaviour. This requires that when the mass is at $X = 0$, the horizontal springs need to be in compression so that $\alpha < 0$. Figure 4a shows a three-dimensional surface plot of the variations of the natural frequency of the linearized system against stiffness parameters α and β. For better clarity, Figure 4b plots two-dimensional curves with the points (α, β) on each of them corresponding to systems of the same linearized natural frequency. Clearly, Ω_n is smaller than 1 when α is negative and is larger than 1 when α becomes positive. This indicates that by adjusting the initial deflection of the horizontal springs as well as the stiffness ratio of the springs, it is possible to achieve a lower or higher natural frequency compared to that of the conventional linear isolator.

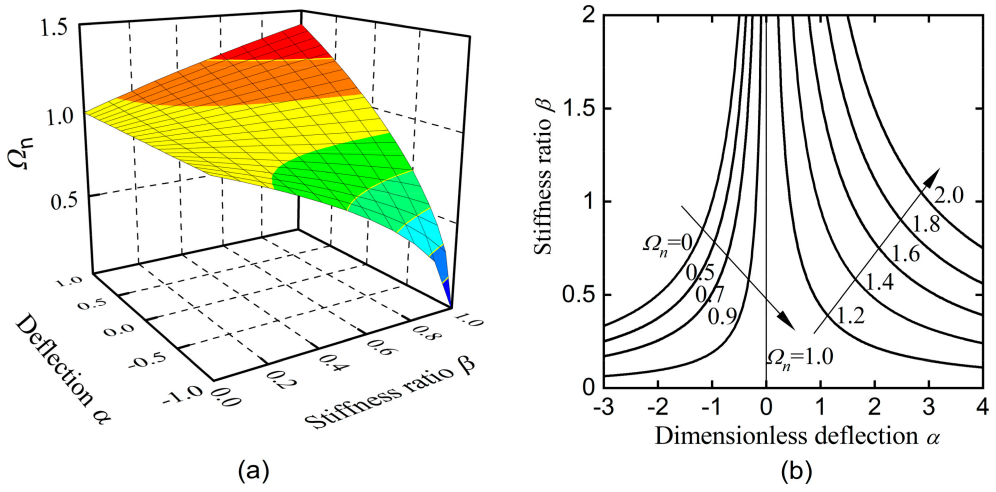

Figure 4. Natural frequency of the linearized system; (**a**) 3–dimensional and (**b**) 2–dimensional plots.

2.3. Stability Analysis

To assist in further analysis, Equation (8) is written in the form of state–space representation as

$$\begin{pmatrix} X' \\ Y' \end{pmatrix} = \begin{pmatrix} Y \\ F_0 cos\ \Omega\tau - 2\xi Y - (1-\beta)X - \beta(1+\alpha)\frac{X}{\sqrt{1-X^2}} \end{pmatrix}. \tag{12}$$

The equilibrium points of the unforced system $(F_0 = 0)$ can be obtained by letting $X' = Y' = 0$:

$$(X_0, Y_0) = (0,\ 0) \text{ and } (X_{1,2}, Y_{1,2}) = \left(\pm\sqrt{1 - \beta^2\left(\frac{1+\alpha}{1-\beta}\right)^2}, 0 \right),\ (\beta \neq 1). \tag{13}$$

While (X_0, Y_0) always exists for varying α and β, the latter two points $(X_{1,2}, Y_{1,2})$ exist only when $0 < \frac{\beta(1+\alpha)}{1-\beta} < 1$. The stability of these equilibria can be assessed by studying the corresponding Jacobian matrix of Equation (12):

$$A = \begin{bmatrix} 0 & 1 \\ -\beta(1+\alpha)(1-X^2)^{-\frac{3}{2}} - (1-\beta) & -2\xi \end{bmatrix}. \tag{14}$$

The characteristic equation of matrix A is

$$\lambda^2 + 2\xi\lambda + \beta(1+\alpha)\left(1-X^2\right)^{-\frac{3}{2}} + (1-\beta) = 0. \tag{15}$$

By investigating the signs of the real part of the solutions to this equation, the stability of the equilibrium points can be determined. Using this and the total number of equilibria, the bifurcation sets of the unforced system are obtained and shown in Figure 5, where the entire parameter region is divided into four sub-regions by lines ACE and BCD. The former line is defined by $\alpha\beta = -1$ with $\Omega_n = 0$ and the latter by $\alpha = -1$, representing linear systems. Bifurcation occurs when crossing either of these two lines. Table 1 shows different types of systems categorized by parameters α and β. As shown previously in Equation (11), as β remains positive, a linearized natural frequency lower than 1 requires $\alpha < 0$. However, systems satisfying this condition may either be due to softening stiffness in Region I to hardening stiffness in Region II, to a double-well potential in Region III, or to a single hump in the potential energy in Region IV. In contrast, the previous NSM study only exhibited the softening stiffness characteristic. Therefore, with a prescribed design natural frequency or a fixed product $\alpha\beta$, the relative values of α and β should still be selected carefully with careful consideration of the stiffness characteristics. For example, for the softening stiffness systems, the mass should not deflect beyond the unstable equilibrium points $(X_{1,2}, Y_{1,2})$ so as to avoid reaching $X = \pm 1$ [14]. Similarly, the systems in Region IV are unstable and thus not useful for vibration isolation.

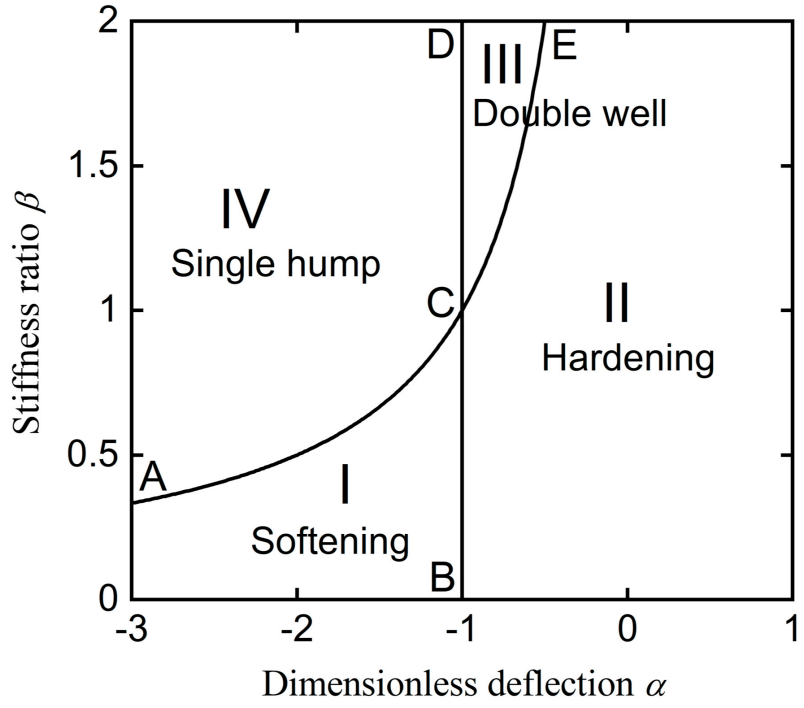

Figure 5. The bifurcation set of the unforced system.

Table 1. Different categories of the system.

Locations of (α, β)	Parameter Values	System Characteristics
Line ACE	$\alpha\beta = -1$	$\Omega_n = 0$
Line BCD	$\alpha = -1$	Linear system
Region I	$\alpha\beta > -1, \alpha < -1$	Softening stiffness system
Region II	$\alpha\beta > -1, \alpha > -1$	Hardening stiffness system
Region III	$\alpha\beta < -1, \alpha > -1$	Double-well potential system
Region IV	$\alpha\beta < -1, \alpha < -1$	Single-hump potential system

2.4. Frequency Response Function

For periodic oscillations around the equilibrium position $X = 0$, the method of averaging [38] can be used for a first-order approximation of the response in the steady state. For its implementation, it is first assumed that the steady-state displacement is $X = r\cos(\Omega\tau + \phi)$ and that the corresponding velocity is $Y = -r\Omega\ \sin(\Omega\tau + \phi)$, where r and ϕ are the response amplitude and the phase angle, respectively. Equation (12) is then transformed into

$$\begin{pmatrix} \cos(\Omega\tau+\phi) & -r\sin(\Omega\tau+\phi) \\ -\Omega\sin(\Omega\tau+\phi) & -r\Omega\cos(\Omega\tau+\phi) \end{pmatrix}\begin{pmatrix} r' \\ \phi' \end{pmatrix} = \begin{pmatrix} 0 \\ f_1 \end{pmatrix}, \tag{16}$$

where

$$f_1 = F_0\cos\Omega\tau + 2r\xi\Omega\sin(\Omega\tau+\phi)\ +\ r\Omega^2\cos(\Omega\tau+\phi) - r\cos(\Omega\tau+\phi)\Delta, \tag{17}$$

$$\Delta = 1 - \beta + \frac{\beta(1+\alpha)}{\sqrt{1 - r^2\cos^2(\Omega\tau+\phi)}}. \tag{18}$$

A manipulation of Equations (17) and (18) leads to the following expressions of the derivatives of the response amplitude and the phase angle:

$$r' = -\frac{1}{\Omega}f_1\sin(\Omega\tau+\phi), \tag{19}$$

$$\phi' = -\frac{1}{r\Omega}f_1\cos(\Omega\tau+\phi). \tag{20}$$

According to the averaging method, the values of r' and ϕ' can be approximated by their average values over a period of the excitation load so that

$$r' = -\frac{\Omega}{2\pi}\int_0^{\frac{2\pi}{\Omega}}\frac{1}{\Omega}f_1\sin(\Omega\tau+\phi)\mathrm{d}\tau, \tag{21}$$

$$\phi' = -\frac{\Omega}{2\pi}\int_0^{\frac{2\pi}{\Omega}}\frac{1}{r\Omega}f_1\cos(\Omega\tau+\phi)\mathrm{d}\tau. \tag{22}$$

By further simplifying Equations (21) and (22), we obtain

$$r' = -\frac{1}{2\Omega}F_0\sin\phi - r\xi, \tag{23}$$

$$r\phi' = -\frac{1}{2\Omega}F_0\cos\phi - \frac{r\Omega}{2} + \frac{(1-\beta)r}{2\Omega} + \frac{2\beta(1+\alpha)}{\pi\Omega r}[K(r) - E(r)], \tag{24}$$

where $K(r)$ and $E(r)$ represent the first and second complete elliptic integrals, respectively [39]. By setting $r' = \phi' = 0$ in Equations (23) and (24) and by cancelling out the phase angle ϕ, the relationship between the system parameters and response amplitude is obtained as

$$F_0^2 = (2\xi\Omega r)^2 + \left\{\left(\Omega^2 - 1 + \beta\right)r - \frac{4\beta(1+\alpha)}{\pi r}[K(r) - E(r)]\right\}^2 \tag{25}$$

When the system parameters are known, Equation (25) can be solved by using a bisection method [40]. Figure 6 compares the obtained results based on the averaging approximations with those obtained using the numerical time-marching Runge–Kutta method. A good agreement between the analytical and numerical results is observed; thus, the averaging formulations are verified. In Figure 6a, four sets of parameters with $(\alpha,\ \beta) = (-1.5,\ 0.5)$, $(-1.25,\ 0.6)$, $(-1,\ 0.75)$, and $(-0.5,\ 1.5)$ are considered. The product $\alpha\beta$ is kept as -0.75. The other parameters are set as $\xi = 0.015$, $F_0 = 0.01$. Essentially, the variations in the combinations of α and β change the system from being that of a softening stiffness system for the first two parameter sets to a linear system and then finally to a hardening stiffness system. Correspondingly, the figure shows that the resonant peak bends to the low-frequency range for the softening stiffness systems and to high frequencies for the hardening stiffness system. It shows that the response peak of the softening systems

is larger than that of the linear and the hardening systems. Away from the resonance region, the amplitude r is not sensitive to the variations in α and β. Figure 6b examines the system responses when $(\alpha,\ \beta) = (-1.2,\ 0.7)$, $(-1.6,\ 0.4)$, $(-1,\ 0.36)$, and $(0.2,\ 2.2)$. The product $\alpha\beta$ varies from -0.84 to -0.64 to -0.36 and then to 0.44. The figure shows a shift of the resonance peak, which is due to the corresponding changes in the linearized natural frequency from 0.4 to 0.6 to 0.8 and then to 1.2. It can be seen that the resonance peak reduces with the natural frequency. In the low-frequency range, a lower natural frequency leads to a larger response amplitude. In contrast, for a large excitation frequency Ω, the response amplitude r is the almost same, and the curves tend to coincide with each other.

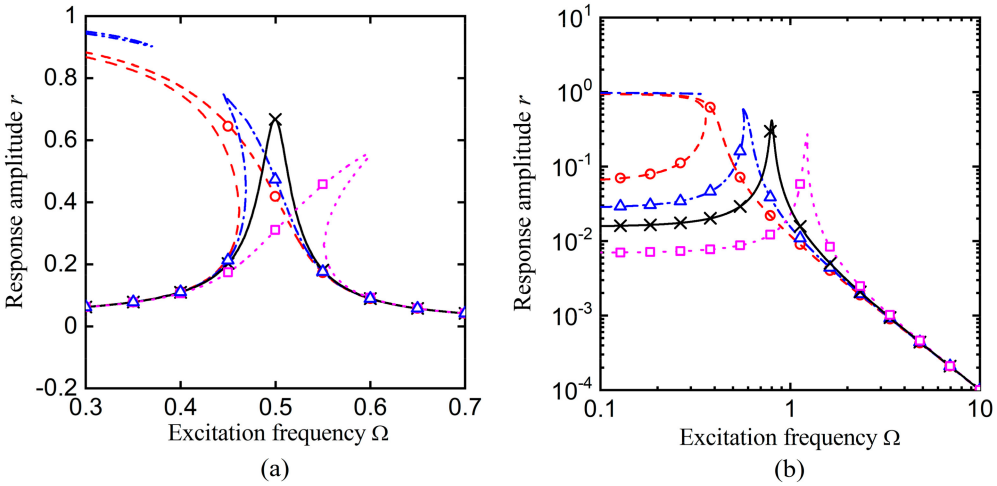

Figure 6. Frequency response curves of systems with (**a**) a fixed product $\alpha\beta$ and (**b**) a varying product $\alpha\beta$ with $\xi = 0.015, F_0 = 0.01$. The dashed, dash–dot, solid, and dotted lines in (**a**) are for $(\alpha,\ \beta) = (-1.5,\ 0.5)$, $(-1.25,\ 0.6)$, $(-1,\ 0.75)$, and $(-0.5,\ 1.5)$, respectively, while in (**b**), the lines are for $(\alpha,\ \beta) = (-1.2,\ 0.7)$, $(-1.6,\ 0.4)$, $(-1,\ 0.36)$, and $(0.2,\ 2.2)$, respectively. Circles, triangles, crosses, and squares denote the corresponding numerical results.

The parameters set in Region III of Figure 5 yield systems of double-well potentials. This kind of system can exhibit chaotic motion, as seen by the bifurcation diagrams in Figure 7 when $\xi = 0.02, \alpha = -0.55, \beta = 2, F_0 = 0.05$. Figure 7a,b presents low-to-high and high-to-low frequency sweepings of the displacement, respectively. The steady-state non-dimensional displacement $X_s(T_s)$ of the mass at sampling time $T_s = T_i + 2(n-1)\pi/\Omega$ is recorded, where T_i is the pre-iteration time. Note that for a periodic response, there will only be finite points shown in the bifurcation diagram at the particular frequency. For the current system with the prescribed parameters, the corresponding pattern of the bifurcation diagram is similar to that of the Duffing oscillator with double-well potential. Figure 7b indicates that the system can exhibit possible chaotic motion when Ω is lower than 0.28 as well as when Ω is located in the range between 0.60 and 0.87. In terms of vibration isolation, chaotic motion is generally considered undesirable. As there are infinite frequency signals in the chaotic response, the traditional force transmissibility is not suitable to reflect the vibration isolation effectiveness. Vibration power flow provides a good indicator of vibration isolation by effectively quantifying the amount of energy input, transmission, and dissipation associated with both periodic and non-periodic chaotic responses [29].

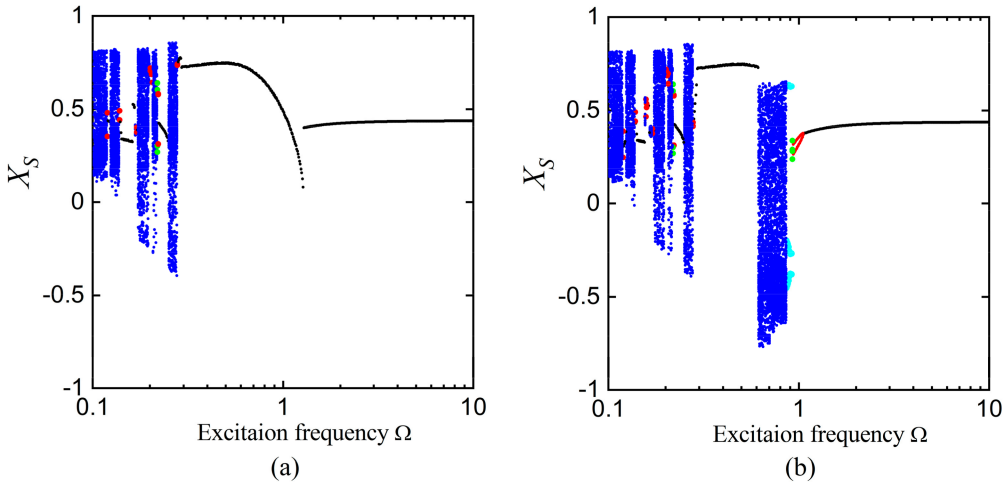

Figure 7. Possible chaotic motions of the double–well potential system $\xi = 0.02$, $\alpha = -0.55$, $\beta = 2$, $F_0 = 0.05$. (**a**) Sweeping from low to high frequencies and (**b**) sweeping from high to low frequencies. Period–1 (black), period–2 (red), period–3 (cyan), period–4 (green), and chaotic motion (blue).

3. Force Transmission and Power Flow Analysis

3.1. Force Transmisibillity

Equation (25) may be rearranged to obtain the nonlinear receptance function of the system:

$$\frac{r}{F_0} = \frac{1}{\sqrt{(2\xi\Omega)^2 + \left\{\Omega^2 - 1 + \beta - \frac{4\beta(1+\alpha)}{\pi r^2}[K(r) - E(r)]\right\}^2}}, \tag{26}$$

which represents the response amplitude of the system per unit excitation force. Note that this function depends on the response amplitude r when $\alpha \neq -1$, different from the receptance functions of linear systems.

To evaluate the performance of vibration isolators, a conventional index is force transmissibility. For the current system, the non-dimensional transmitted force from the mass to base point D is

$$f_{t1} = 2\xi X' + X. \tag{27}$$

When a first-order approximation of response $X = r\cos(\Omega T + \phi)$ is assumed, the amplitude of this transmitted force is

$$|f_{t1}| = r\sqrt{(2\xi\Omega)^2 + 1}. \tag{28}$$

The force transmissibility of the system can be approximated by

$$TR = \frac{r}{F_0}\sqrt{(2\xi\Omega)^2 + 1}, \tag{29}$$

which is the $\sqrt{(2\xi\Omega)^2 + 1}$ times of the receptance function shown by Equation (26).

Figure 8 provides the plots of the defined receptance function r/F_0 and the transmissibility TR against the excitation frequency Ω. For five sets of parameters $\alpha = -1.2$, $\beta = 0.7$ (Case one), $\alpha = -1.6$, $\beta = 0.4$ (Case two), $\alpha = -1$, $\beta = 0.36$ (Case three), $\alpha = 0.2$, $\beta = 2.2$ (Case four), and $\alpha = 0.5$, $\beta = 2.5$ (Case five), the corresponding natural frequencies of the linearized system are 0.4, 0.6, 0.8, 1.2, and 1.5, respectively. The damping ratio ξ is fixed as 0.01. Cases one and two refer to softening stiffness systems, while Cases four and five correspond to hardening stiffness systems. On each surface, there is a peak curve, which can be described mathematically by examining the minimum condition of the denominator of the expression on the right-hand side of Equation (26) [14]. For Cases one and two, the surface shifts and bends to the low-frequency range. This is beneficial for vibration isolation, as there is a larger frequency range of effective isolation. At high excitation

frequencies, the surfaces merge with each other, and r/F_0 and TR become insensitive to the nonlinear parameters α and β.

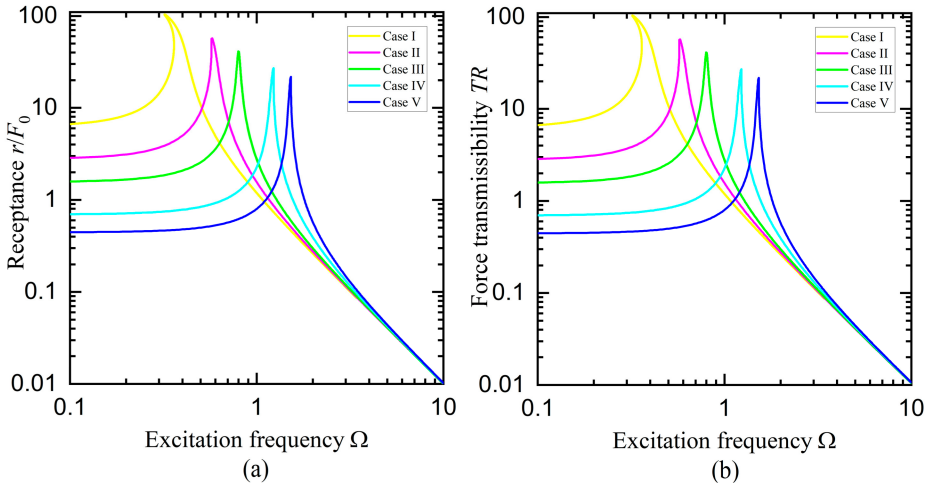

Figure 8. (**a**) Receptance function r/F_0 of the system and (**b**) force transmissibility TR with $\xi = 0.01$. The yellow, magenta, green, cyan and blue surfaces correspond to Case one, two, three, four, and five, respectively.

Figure 9 shows the force transmission behaviour of the proposed SBM design (Case three: $\alpha = -1$ and $\beta = 0.36$), the analogical NSM design [14] ($\alpha = 2P/kl = 0.02$, damping and external force are the same as Case three), and the linear spring-damper isolator (i.e., $\beta = 0$). For the conventional NSM, negative stiffness is obtained by applying constant compression forces at the ends of the bars, while variable spring forces are used for the same purpose in the current SBM. Figure 9a presents that the resonant peak of the TR curve shifts to lower frequencies compared to the conventional linear and the NSM cases, thereby expanding the effective isolation range. In the high-frequency range, three different isolators have similar force transmission performance. Figure 9b shows the time history of the steady-state transmitted force f_{t1} within four periodic cycles. When the excitation frequency $\Omega = 1$, the force amplitudes are approximately equal to 0.33, 0.050, and 0.029 for the linear, the referenced NSM and the proposed SBM cases, respectively. This indicates that the SBM in the proposed isolator can effectively reduce the force transmission level near the original resonance.

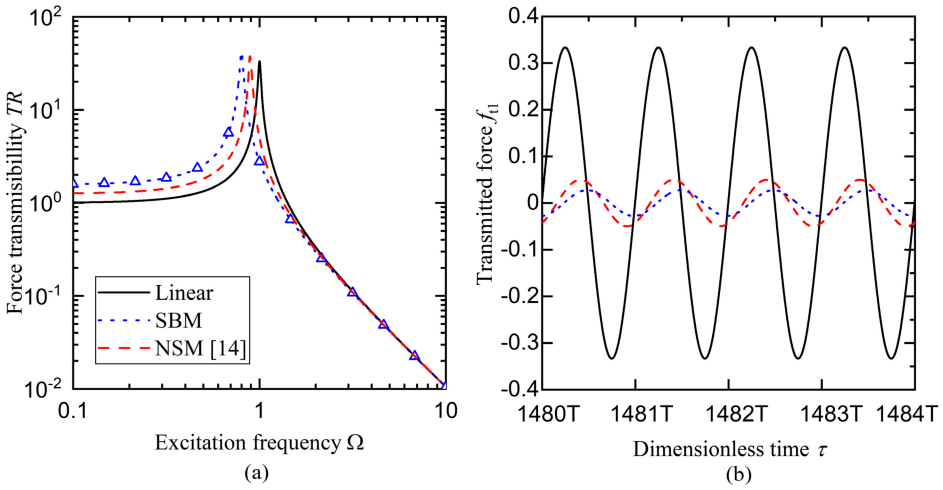

Figure 9. Force transmission performance of the SBM, the analogical NSM [14], and the linear isolator in terms of the (**a**) force transmissibility TR and (**b**) time histories of the transmitted force f_{t1}. Parameter values $\alpha = -1$, $\beta = 0.36$, $\xi = 0.01$, $F_0 = 0.01$.

3.2. Time-Averaged Input Power and Kinetic Energy

The time-averaged dissipated and input powers in the system over the time span τ_p are

$$\overline{p}_{\mathrm{d}} = \frac{1}{\tau_p}\int_{\tau_0}^{\tau_0+\tau_p} p_{\mathrm{d}}\mathrm{d}\tau,\ \overline{p}_{\mathrm{in}} = \frac{1}{\tau_p}\int_{\tau_0}^{\tau_0+\tau_p} p_{\mathrm{in}}\mathrm{d}\tau, \tag{30}$$

Respectively, where $p_d = 2\xi X'X'$ is the dissipated power and $p_{\mathrm{in}} = X'F_0\cos\Omega\tau$ is the input power, τ_0 is starting time of the integral, and τ_p is the integral time period, which equals one excitation cycle, i.e., $\tau_p = 2\pi/\Omega$.

When a first-order approximation of the response is used, the velocity of the mass is $Y = -r\Omega\sin(\Omega T + \phi)$. Consequently, the time-averaged input power over a cycle of oscillation $2\pi/\Omega$ is

$$\overline{p}_{\mathrm{in}} = -\frac{r\Omega F_0}{2}\sin\phi. \tag{31}$$

Replacing $\sin\phi$ in Equation (31) using Equation (23) and further simplifying, the time-averaged input power is rewritten as

$$\overline{p}_{\mathrm{in}} = \xi r^2\Omega^2 = \overline{p}_{\mathrm{d}}. \tag{32}$$

Equation (32) shows that the time-averaged input power is equal to the time-averaged dissipated power within one excitation cycle, indicating that total external power input is consumed by the viscous damping.

The maximum kinetic energy of the system in the steady-state motion is encountered when the mass has the maximum speed of $|V_{max}| = r\Omega$, so that

$$K_{\max} = \frac{1}{2}r^2\Omega^2 = \frac{\overline{p}_{\mathrm{in}}}{2\xi}. \tag{33}$$

Note that from Equations (25), (32), and (33), $\overline{p}_{\mathrm{in}}$ and $K_{\max}$ are re-expressed as

$$\overline{p}_{\mathrm{in}} = \frac{\xi F_0^2}{4\xi^2 + \left\{\frac{\Omega^2-1+\beta}{\Omega} - \frac{4\beta(1+\alpha)}{\pi r^2\Omega}[K(r)-E(r)]\right\}^2}, \tag{34}$$

$$K_{\max} = \frac{0.5F_0^2}{4\xi^2 + \left\{\frac{\Omega^2-1+\beta}{\Omega} - \frac{4\beta(1+\alpha)}{\pi r^2\Omega}[K(r)-E(r)]\right\}^2}, \tag{35}$$

respectively, from which we have

$$\overline{p}_{\mathrm{in}} \le \frac{F_0^2}{4\xi},\ K_{\max} \le \frac{F_0^2}{8\xi^2}. \tag{36}$$

These two expressions show the existence of an upper bound power flow values, which only depend on the damping ratio ξ and the excitation amplitude F_0. The upper bound is only reached when the terms in the curly brackets of Equations (34) and (35) vanish:

$$\Omega^2 - 1 + \beta - \frac{4\beta(1+\alpha)[K(r)-E(r)]}{\pi r^2} = 0. \tag{37}$$

With reference to the frequency–response relationship in Equation (25) to replace Ω, a nonlinear equation of response amplitude r can be established:

$$F_0^2 = 4\xi^2 r^2\left(1 - \beta + \frac{4\beta(1+\alpha)[K(r)-E(r)]}{\pi r^2}\right), \tag{38}$$

It is the feasible solutions of which that provide the response amplitude r corresponding to the upper bound value. Together with Equation (38), responses with maximum time-averaged power flow can be identified. The upper bound value cannot be achieved if there is no solution to the equation. Additionally, it can be seen from Equations (34) and (35) that in the high-frequency range where Ω is large, the following approximations may be made:

$$\overline{p}_{\mathrm{in}} \approx \frac{\xi F_0^2}{4\xi^2 + \Omega^2},\quad K_{\max} \approx \frac{0.5F_0^2}{4\xi^2 + \Omega^2} \tag{39}$$

Thus, the time-averaged input power and kinetic energy become independent of the stiffness parameters α and β at large excitation frequencies.

To obtain the transient response and power flow variables, Equation (8) is first transformed into two first-order differential equations. Then, the Runge–Kutta method based numerical integrations is used for solutions. By using this method, Figure 10 shows the input power behaviour of the system with $\alpha = -0.55$, $\beta = 2, \xi = 0.02$, and $F_0 = 0.05$, with the excitation frequency Ω taken as 0.5 in Figure 10a–c and 0.8 in Figure 10d–f, respectively. It is shown in Figure 7 that at those two frequencies, the system will exhibit periodic and chaotic motion, respectively. Figure 10a shows that input power p_{in} is periodic and that its dominant frequency is located at the excitation frequency 2Ω. This is due to the trigonometric product of the response velocity and the excitation. Figure 10d shows that when chaos occurs, the time series of p_{in} exhibits an irregular, random-like behaviour. Figure 10e and f further shows infinite frequency components in both p_{in} and the displacement X. The dominant components in X are located at Ω and $\Omega/3$. Consequently, there are high spikes in the spectrum of p_{in} at $2\Omega/3$, $4\Omega/3$, and 2Ω.

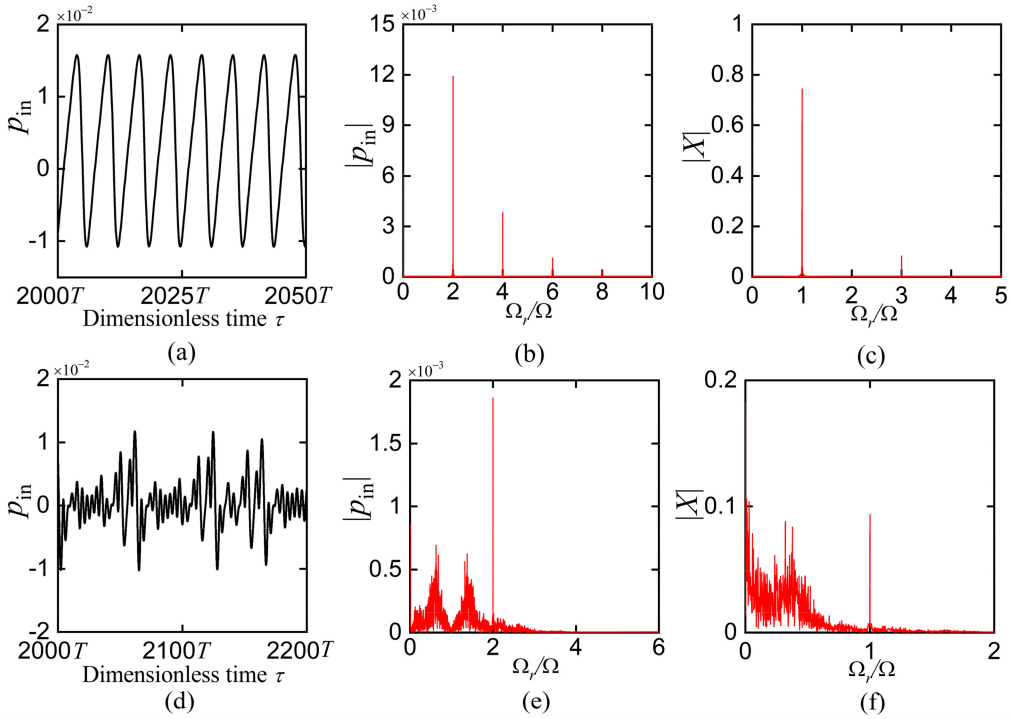

Figure 10. Instantaneous input power. Parameters $\alpha = -0.55$, $\beta = 2, \xi = 0.02, F_0 = 0.05$, and (**a**–**c**) $\Omega = 0.5$, period–1 motion; (**d**–**f**), $\Omega = 0.8$, chaotic motion. (**a**, **d**) are for transient input power; (**b**, **e**) are the frequency components in p_{in}; (**c**, **f**) show the frequency components in displacement.

Using the averaging formulation as well as numerical integrations, the effects of parameters α and β on the power flows of the system are examined and shown in Figures 11 and 12. In the following content, the power flow variables are presented in decibel scales with a reference level of 10^{-12}. In Figure 11, the system changes from being of softening stiffness when $(\alpha, \beta) = (-1.5, 0.5)$ or $(-1.25, 0.6)$ to being linear when $(\alpha, \beta) = (-1, 0.75)$ and then to being of hardening stiffness when $(\alpha, \beta) = (-0.5, 1.5)$. The other parameters are set as $\xi = 0.01$, $F_0 = 0.01$. For all of these cases, the product of α and β remains -0.75 so that the natural frequency of the linearized system remains unchanged at 0.5. It can seen that the peaks in the power flow curves bend to the low-frequency range for softening systems and to the high-frequency range when the system is of hardening stiffness. The power flow curves for the $(\alpha, \beta) = (-1.5, 0.5)$ case are continuous with the peak values being lower than the case with $(\alpha, \beta) = (-1.25, 0.6)$. This indicates a potential benefit of using softening stiffness to reduce the peak time-averaged power flows. The

time-averaged input power and the maximum kinetic energy for linear and the hardening cases are approximately of the same height. As Ω moves away from the resonance region, the curves for different combinations of α and β coincide, and the power flow levels are approximately the same. This results from the fact that the response amplitude at these frequencies is small, so the nonlinear stiffness effects are insignificant.

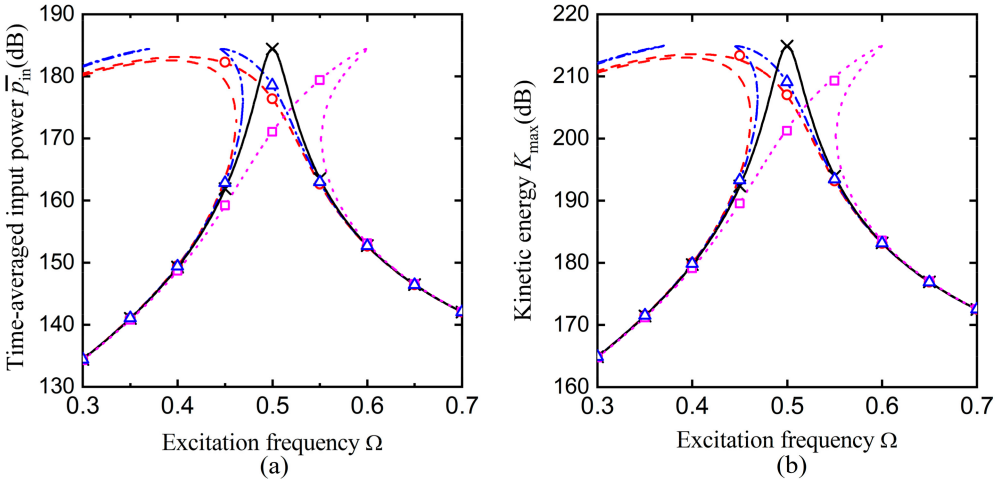

Figure 11. Effects of different combination of α and β with a fixed product on (**a**) the time–averaged input power and (**b**) the maximum kinetic energy. Dashed, solid line, dash–dot, and dotted lines for $(\alpha,\ \beta) = (-1.5,\ 0.5)$, $(-1.25,\ 0.6)$, $(-1,\ 0.75)$, and $(-0.5,\ 1.5)$, respectively. Circles, triangles, crosses, and squares denote the corresponding numerical results.

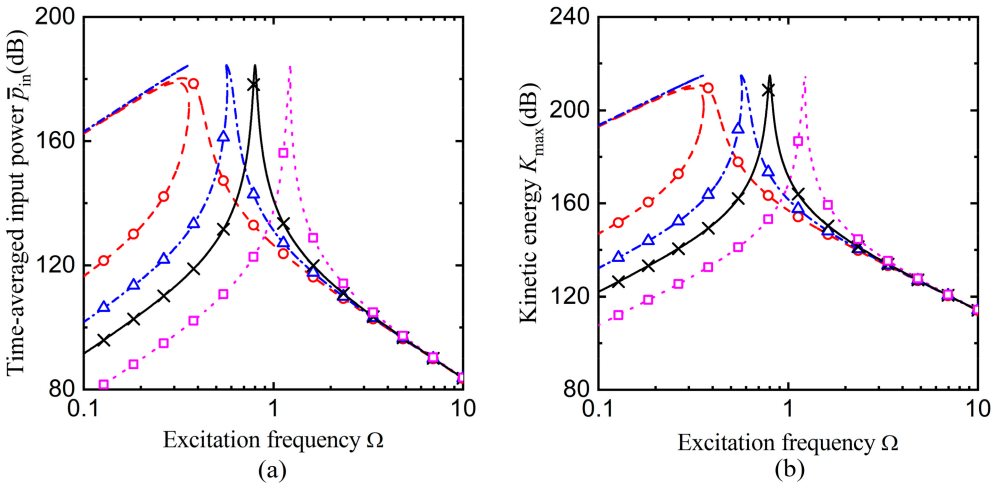

Figure 12. Effects of a varying product $\alpha\beta$ on (**a**) the time-averaged input power and (**b**) the maximum kinetic energy ($\xi = 0.015$, $F_0 = 0.01$). Dashed, solid line, dash–dot, and dotted lines for $(\alpha,\ \beta) = (-1.2,\ 0.7)$, $(-1.6,\ 0.4)$, $(-1,\ 0.36)$, and $(0.2,\ 2.2)$, respectively. Circles, triangles, crosses, and squares denote the corresponding numerical results.

Figure 12 presents the power flows of systems with different products of α and β. The system changes from being one with softening stiffness when $(\alpha,\ \beta) = (-1.2,\ 0.7)$ or $(-1.6,\ 0.4)$ to being linear when $(\alpha,\ \beta) = (-1,\ 0.36)$ and then having a hardening characteristic when $(\alpha,\ \beta) = (0.2,\ 2.2)$. The other parameters are set as $\xi = 0.015$, $F_0 = 0.01$. The natural frequency Ω_n of the linearized system varies from 0.4 to 0.6 to 0.8 and then to 1.2. The figure shows that with a small product of α and β, the peaks in the power flow curves shift to the low-frequency range. This is good for vibration isolation, as the amount of the input power of the system is low over a larger range of excitation frequencies. At low excitation frequencies, a smaller value of $\alpha\beta$ results in a larger amount

of time-averaged input power and also a higher level of maximum kinetic energy. It is seen that the peak values of $\overline{p}_{\text{in}}$ and $K_{\max}$ of the softening system with $(\alpha,\ \beta) = (-1.2,\ 0.7)$ are lower than those of the other cases. Again, this characteristic may be used to enhance vibration isolation. When the excitation frequency Ω becomes large, there is little difference in the values of $\overline{p}_{\text{in}}$ and $K_{\max}$ for the examined sets of stiffness parameters α and β. This can be explained by Equation (39), i.e., the time-averaged power flow variables are not sensitive to the variations of the stiffness parameters in the high–frequency range.

3.3. Non-Periodic Response

In the previous content, the power flow behaviour of the system with periodic responses was examined. It is noted that when stiffness nonlinearities are introduced by the SBM, the steady-state response may become non-periodic or even chaotic. The performance of the vibration isolation system exhibiting non-periodic motions is unclear and investigated herein.

To examine the dynamic behaviour of the system over a large frequency range, numerical simulations based on the fourth-order Runge–Kutta method were conducted. For each interested value of excitation frequency, the steady-state displacement response was sampled over each cycle of excitation. In this way, by plotting the sampling point positions against the frequency, the response characteristics can be shown. Based on this, Figures 13 and 14 show the response behaviour and the associated time-averaged power flow of a system with the parameters set as $\alpha = -0.7$, $\beta = 1.5$, $\xi = 0.015$, $F_0 = 0.01$. Figure 13a shows that non-periodic responses can be encountered in frequency bands located between 0.125 and 0.142. There are also period-2 motions in frequency range B from $\Omega = 0.645$ to $\Omega = 0.70$, with the period of the response being twice that of the excitation. The corresponding time-averaged input power to these responses is shown in Figure 13b. To reflect the long-time steady-state dynamic behaviour of the system, the starting time τ_0 and the averaging time τ_p are set as 500 and 1000 cycles of the excitation, respectively. The results shown in Figure 13b indicate that the level of the time-averaged input power of the non-periodic responses in frequency band A is similar to that of the periodic responses near the band. A jump in the time-averaged input power occurs when $\Omega = 0.4$ with the response bifurcates from motions across two potential wells to a single-well motion. In the higher frequency range B with the system exhibiting period-2 response motions, the time-averaged input power is larger than the period-1 responses encountered close to the frequency band. Figure 13 shows that the bifurcation diagrams of the displacement response and input power can present different quantification outcomes; therefore, it is necessary to assess the level of vibration transmission and isolation performance from the two aspects of displacement and energy.

In Figure 14, the system parameters and numerical settings remain the same as those used in Figure 14, but the excitation frequency varies from 10 to 0.1 to follow the response branches from high to low frequencies. Comparing this figure with Figure 13, it can be seen that there is a coexistence of the period-1 and period-2 responses from $\Omega = 0.57$ to $\Omega = 0.645$. This is mainly due to the different initial conditions in low-to-high and high-to-low sweeping. Additionally, non-periodic responses appear from $\Omega = 0.29$ to $\Omega = 0.35$, where period-1 responses were observed in the same region in Figure 13. Clearly, these multiple solutions of the system arise from the stiffness nonlinearity of the SBM. A jump up in time-averaged input power is encountered at $\Omega = 0.29$, with the system motion changing from being non-periodic to being periodic. In high-frequency range, Figures 13 and 14 show the same results, which means that the displacement and power flow behaviour are not sensitive to the initial conditions when the excitation frequency is large.

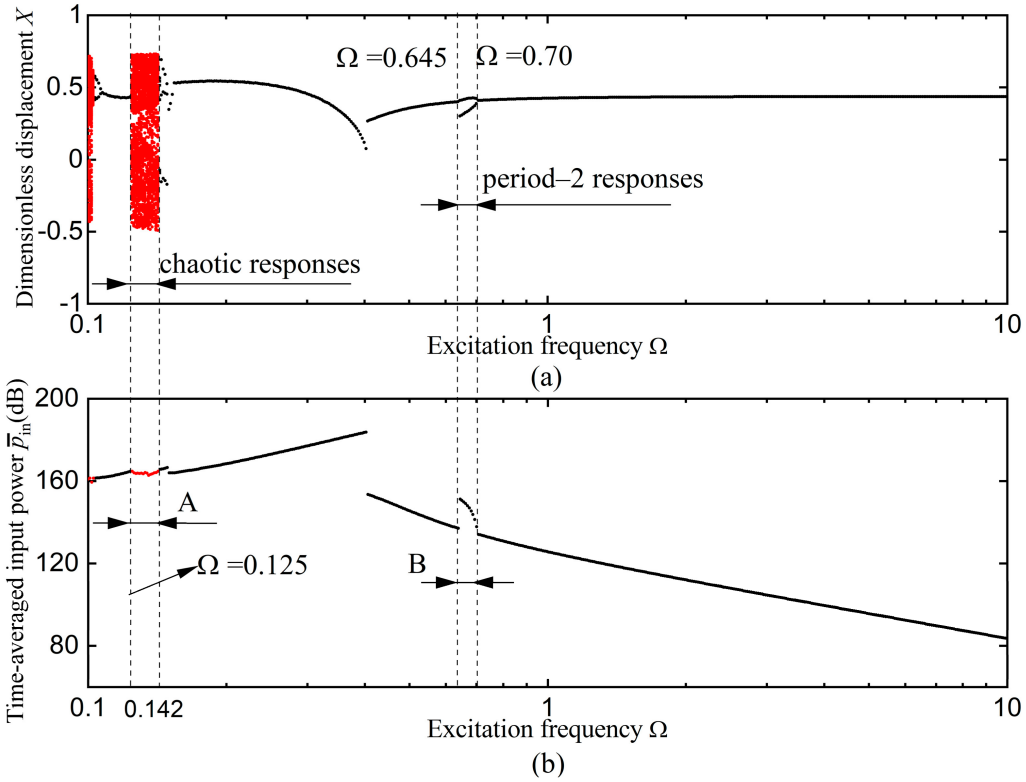

Figure 13. Bifurcation diagrams of (**a**) displacement response and (**b**) time–averaged input power with low to high excitation frequencies.

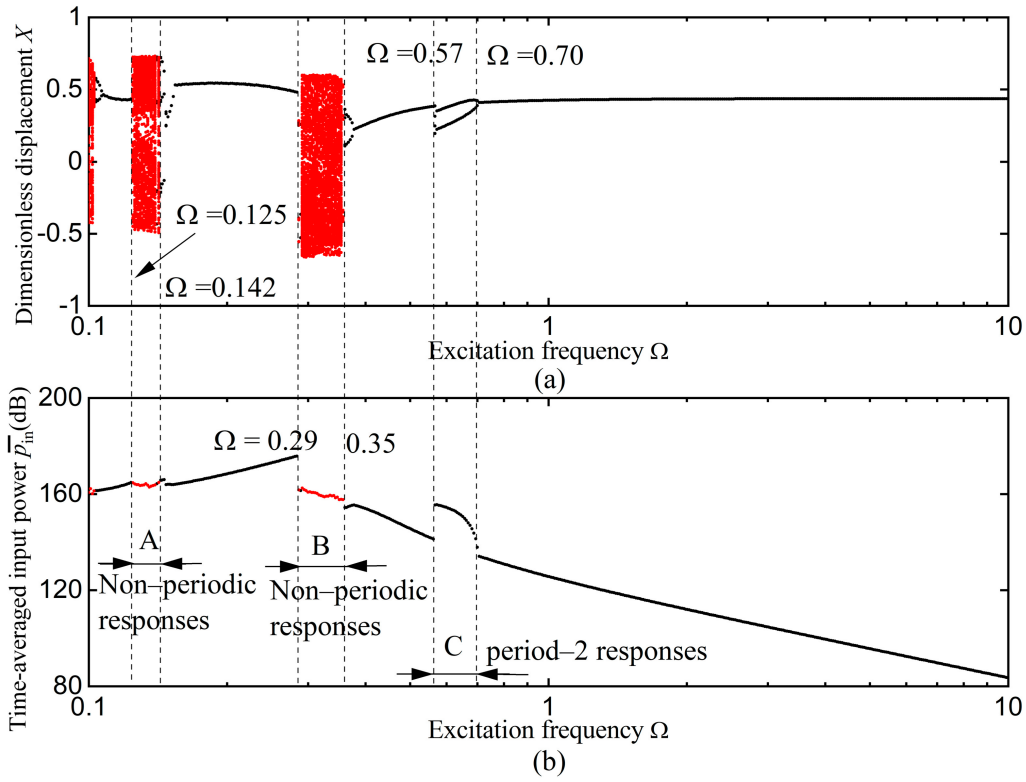

Figure 14. Bifurcation diagrams of (**a**) displacement response and (**b**) time–averaged input power with high to low excitation frequencies.

To examine whether the non-periodic responses are chaotic, the corresponding Lyapunov exponent can be calculated [41]. This quantity has been widely used in the identification of chaotic responses by evaluating the rate of separation of nearby trajectories. A positive Lyapunov exponent indicates the occurrence of chaotic motions. For a system with $\alpha = -0.7$, $\beta = 1.5$, $\xi = 0.015$, $\Omega = 0.3$ and the initial conditions $\left(X_0,\ \dot{X}_0\right) = (0,\ 0)$, the time histories of the steady-state response are obtained by using numerical integrations. A Fourier transformation of the response was performed, and the results shown in Figure 15a demonstrate a broadband frequency spectrum. The largest Lyapunov exponent obtained was 0.049, suggesting that the response is of a chaotic nature. In this situation, the response does not repeat itself at a regular interval, as shown in Figure 15b. As a result, the use of force transmissibility, traditionally defined as the ratio of the amplitudes of the transmitted and the excitation forces, is not suitable. Additionally, when chaos occurs, assessing the performance of the isolator via approximations by only considering the response amplitude can result in large inaccuracies. In contrast, time-averaged power flow variables can provide good performance indices by taking into account of the long-term dynamic behaviour of the system. As shown in Figures 13 and 14, the use of time-averaged input power $\overline{p}_{\text{in}}$ allows quantitative comparisons of the vibration levels associated with periodic and chaotic responses.

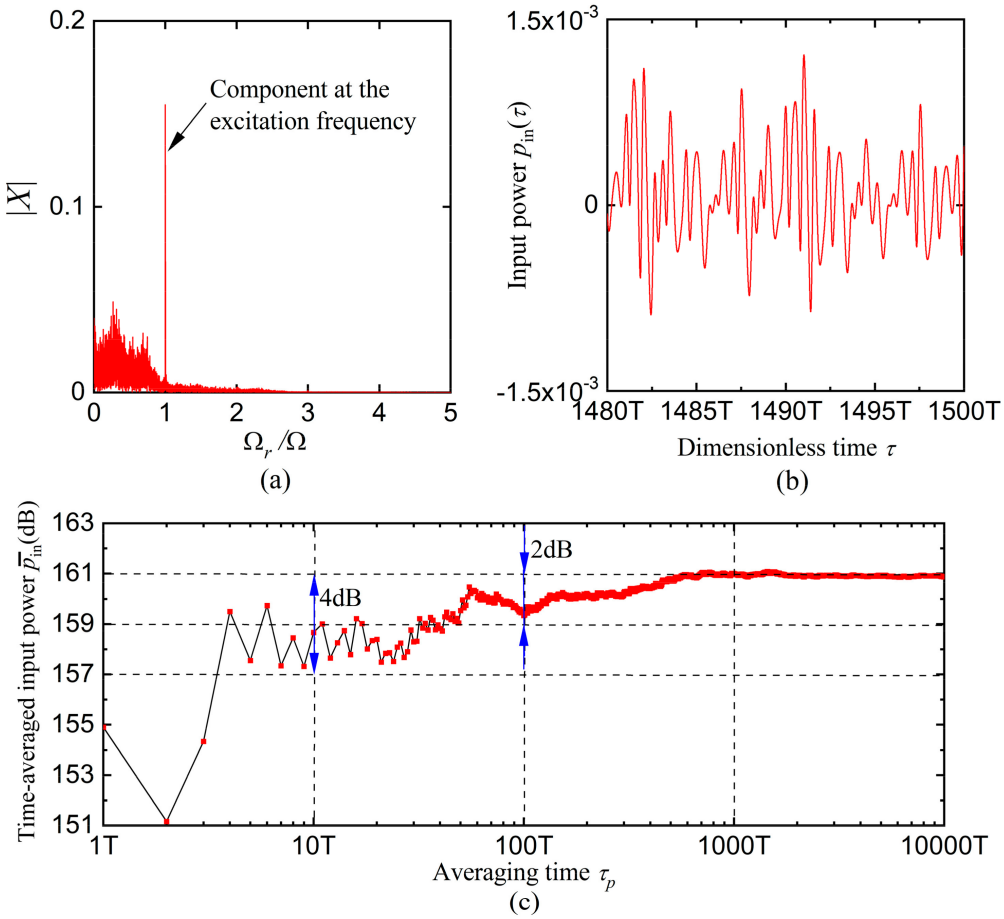

Figure 15. Dynamic response at $\Omega = 0.3$ with $\alpha = -0.7$, $\beta = 1.5$, $\xi = 0.015$, $F_0 = 0.01$. (**a**) Frequency spectrum, (**b**) instantaneous input power, and (**c**) time–averaged input power.

It should be noted that for a robust functioning of $\overline{p}_{\text{in}}$ as a performance index, the effects of averaging time on the time-averaged input power should be examined [29]. For this purpose, an investigation is conducted on the dependence of the time-averaged input power of a chaotic response on the averaging time. The results shown in Figure 15c suggest that the variations of $\overline{p}_{\text{in}}$ are confined to a 4dB band when the averaging time

τ_p is larger than 10 excitation cycles ($10T$) and to a 2dB band when $\tau_p > 100T$. As τ_p increases further, the changes in $\overline{p}_{\text{in}}$ become smaller, and the time-averaged input power evolves asymptotically to 161dB. The asymptotic characteristic of $\overline{p}_{\text{in}}$ can arise from the fact that chaotic responses are bounded in the phase space [42]. This asymptotic behaviour enables quantitative measurements of vibration levels associated with chaotic responses and consequently demonstrates the advantage of using power flow variables as the performance indicators of nonlinear vibration isolators.

4. Conclusions

This study investigated a vibration isolation system consisting of a vertical spring-damper linear isolator unit and a spring-bar mechanism (SBM) created by a pair of bars linked with horizontal springs. The system model was first introduced and was then analysed, both by analytical approximations using the averaging method and by numerical integrations. The performance of the isolator was examined by using both nonlinear force transmissibility as well as the time-averaged power flows and the maximum kinetic energy of the mass. It was shown that the stiffness characteristics of the system can be controlled by two parameters describing the initial compression of the horizontal springs as well as the stiffness ratio of the horizontal and vertical springs. It was found that adding SBM can reduce the natural frequency of the linearized system so as to provide a larger functioning frequency range. Compared to the traditional linear spring-damper isolator and the previous NSM isolator design, the proposed SBM can reduce the force transmission level near the resonance and has a wider effective isolation range. It was also found that different combinations of these parameters may yield different nonlinear effects for enhanced vibration isolation. By adjusting these two parameters, the SBM can also provide a purely linear negative restoring force and thus negative stiffness without introducing possibly harmful nonlinear effects into the system. It was shown that adding the SBM was shown to be beneficial for vibration isolators as both force transmission and the amount of power input were reduced in the high-frequency range. It was found that the system can exhibit chaotic motions, for which the associated time-averaged input power tended to an asymptotic value with increasing averaging time. Thus, time-averaged power flow variables can be used as a uniform index to assess and compare the performance of nonlinear vibration isolation systems exhibiting either periodic or chaotic motions.

Author Contributions: Conceptualization, J.Y.; methodology, B.S. and J.Y.; software, B.S. and J.Y.; validation, B.S. and J.Y.; formal analysis, B.S. and J.Y.; investigation, B.S. and J.Y.; resources, B.S., J.Y. and T.L.; data curation, B.S. and J.Y.; writing—original draft preparation, B.S. and J.Y.; writing—review and editing, J.Y. and T.L.; visualization, B.S. and J.Y.; supervision, J.Y.; project administration, J.Y. and T.L.; funding acquisition, J.Y. and T.L. All authors have read and agreed to the published version of the manuscript.

Funding: This research was funded by the National Natural Science Foundation of China, grant numbers 51839005, 51879113, and 12172185.

Institutional Review Board Statement: Not applicable.

Informed Consent Statement: Not applicable.

Data Availability Statement: Not applicable.

Acknowledgments: We would like to thank the reviewers and the Applied Sciences team for their support.

Conflicts of Interest: The authors declare no conflict of interest.

References

1. Harris, C.M.; Crede, C.E. *Shock and Vibration Handbook*; McGraw-Hill: New York, NY, USA, 1961.
2. Den Hartog, J.P. *Mechanical Vibration*; Dover Publications Inc.: New York, NY, USA, 1985.
3. Yilmaz, C.; Kikuchi, N. Analysis and design of passive band-stop filter-type vibration isolators for low-frequency applications. *J. Sound Vib.* **2006**, *291*, 1004–1028. [CrossRef]

4. Xing, J.T.; Xiong, Y.P.; Price, W.G. Passive-active vibration isolation systems to produce zero or infinite dynamic modulus: Theoretical and conceptual design strategies. *J. Sound Vib.* **2005**, *286*, 615–636. [CrossRef]
5. Alabuzhev, P.; Gritchin, A.; Kim, L.; Migirenko, G.; Chon, V.; Stepanov, P. *Vibration Protecting and Measuring Systems with Quasi-Zero Stiffness*; Hemisphere: New York, NY, USA, 1989.
6. Platus, D.L. Negative-stiffness-mechanism vibration isolation system. In Proceedings of the SPIE-The International Society for Optical Engineering, Vibration Control in Microelectronics, Optics, and Metrology, San Jose, CA, USA, 4–6 November; 1992; pp. 44–54.
7. Carrella, A.; Brennan, M.J.; Waters, T.P. Static analysis of a passive vibration isolator with quasi-zero-stiffness characteristic. *J. Sound Vib.* **2007**, *301*, 678–689. [CrossRef]
8. Lee, C.M.; Goverdovskiy, V.N.; Temnikov, A.I. Design of springs with "negative" stiffness to improve vehicle driver vibration isolation. *J. Sound Vib.* **2007**, *302*, 865–874. [CrossRef]
9. Kovavic, I.; Brennan, M.J.; Waters, T.P. A study of a nonlinear vibration isolator with a quasi-zero stiffness characteristic. *J. Sound Vib.* **2008**, *315*, 700–711. [CrossRef]
10. Lu, Z.Q.; Yang, T.; Brennan, M.J.; Liu, Z.; Chen, L.-Q. Experimental Investigation of a Two-stage Nonlinear Vibration Isolation System with High-static-Low-Dynamic Stiffness. *J. Appl. Mech.* **2017**, *84*, 021001. [CrossRef]
11. Carrella, A.; Brennan, M.J.; Waters, T.P.; Shin, K. On the design of a high-static-low-dynamic stiffness isolator using linear mechanical springs and magnets. *J. Sound Vib.* **2008**, *315*, 712–720. [CrossRef]
12. Lu, Z.Q.; Wu, D.; Ding, H.; Chen, L.-Q. Vibration isolation and energy harvesting integrated in a Stewart platform with high static and low dynamic stiffness. *Appl. Math. Model.* **2021**, *89*, 249–267. [CrossRef]
13. Cao, Q.; Xiong, Y.P.; Wiercigroch, M. A novel model of dipteran flight mechanism. *Int. J. Dynam. Control* **2013**, *1*, 1–11. [CrossRef]
14. Yang, J.; Xiong, Y.P.; Xing, J.T. Dynamics and power flow behaviour of a nonlinear vibration isolation system with a negative stiffness mechanism. *J. Sound Vib.* **2013**, *332*, 167–183. [CrossRef]
15. Lu, Z.Q.; Gu, D.-H.; Ding, H.; Lacarbonara, W.; Chen, L.-Q. Nonlinear vibration isolation via a circular ring. *Mech. Syst. Signal Process.* **2020**, *136*, 106490. [CrossRef]
16. Shaw, A.D.; Neild, S.A.; Wagg, D.J.; Weaver, P.M.; Carella, A. A nonlinear spring mechanism incorporating a bistable composite plate for vibration isolation. *J. Sound Vib.* **2013**, *332*, 65–75. [CrossRef]
17. Yan, B.; Ma, H.; Zhang, L.; Zheng, W.; Wang, K.; Wu, C. A bistable vibration isolator with nonlinear electromagnetic shunt damping. *Mech. Syst. Signal Process.* **2020**, *136*, 106504. [CrossRef]
18. Yan, B.; Ma, H.; Yu, N.; Zhang, L.; Wu, C. Theoretical modeling and experimental analysis of nonlinear electromagnetic shunt damping. *J. Sound Vib.* **2020**, *471*, 115184. [CrossRef]
19. Zhang, L.; Zhao, C.; Qian, F.; Dhupia, J.S.; Wu, M. A Variable Parameter Ambient Vibration Control Method Based on Quasi-Zero Stiffness in Robotic Drilling Systems. *Machines* **2021**, *9*, 67. [CrossRef]
20. Meng, Q.; Yang, X.; Li, W.; Lu, E.; Sheng, L. Research and Analysis of Quasi-Zero-Stiffness Isolator with Geometric Nonlinear Damping. *Shock Vib.* **2017**, *2017*, 1–9. [CrossRef]
21. Tuo, J.; Deng, Z.; Huang, W.; Zhang, H. A six degree of freedom passive vibration isolator with quasi-zero-stiffness-based supporting. *J. Low Freq. Noise Vib. Act. Control* **2018**, *37*, 279–294. [CrossRef]
22. Le, T.D.; Ahn, K.K. A vibration isolation system in low frequency excitation region using negative stiffness structure for vehicle seat. *J. Sound Vib.* **2011**, *330*, 6311–6335. [CrossRef]
23. Goyder, H.G.D.; White, R.G. Vibration power flow from machines into built-up structures. *J. Sound Vib.* **1980**, *68*, 59–117. [CrossRef]
24. Pinnington, R.J.; White, R.G. Power flow through machine isolators to resonant and non-resonant beam. *J. Sound Vib.* **1981**, *75*, 179–197. [CrossRef]
25. Royston, T.J.; Singh, R. Optimization of passive and active non-linear vibration mounting systems based on vibratory power transmission. *J. Sound Vib.* **1996**, *194*, 295–316. [CrossRef]
26. Royston, T.J.; Singh, R. Vibratory power flow through a nonlinear path into a resonant receiver. *J. Acoust. Soc. Am.* **1997**, *101*, 2059–2069. [CrossRef]
27. Zhu, C.; Yang, J.; Rudd, C. Vibration transmission and power flow of laminated composite plates with inerter-based suppression configurations. *Int. J. Mech. Sci.* **2021**, *190*, 106012. [CrossRef]
28. Xiong, Y.P.; Xing, J.T.; Price, W.G. Interactive power flow characteristics of an integrated equipment–nonlinear isolator–travelling flexible ship excited by sea waves. *J. Sound Vib.* **2005**, *287*, 245–276. [CrossRef]
29. Yang, J.; Xiong, Y.P.; Xing, J.T. Nonlinear power flow analysis of the Duffing oscillator. *Mech. Syst. Signal Process.* **2014**, *45*, 563–578. [CrossRef]
30. Yang, J.; Xiong, Y.P.; Xing, J.T. Power flow behaviour and dynamic performance of a nonlinear vibration absorber coupled to a nonlinear oscillator. *Nonlinear Dyn.* **2015**, *80*, 1063–1079. [CrossRef]
31. Yang, J.; Xiong, Y.P.; Xing, J.T. Vibration power flow and force transmission behaviour of a nonlinear isolator mounted on a nonlinear base. *Int. J. Mech. Sci.* **2016**, *115–116*, 238–252. [CrossRef]
32. Yang, J.; Shi, B.; Rudd, C. On vibration transmission between Interactive oscillators with nonlinear coupling interface. *Int. J. Mech. Sci.* **2018**, *137*, 238–251. [CrossRef]

33. Shi, B.; Yang, J.; Rudd, C. On vibration transmission in oscillating systems incorporating bilinear stiffness and damping elements. *Int. J. Mech. Sci.* **2019**, *150*, 458–470. [CrossRef]
34. Shi, B.; Yang, J. Quantification of vibration transmission between coupled nonlinear oscillators. *Int. J. Dynam. Control* **2020**, *8*, 418–435. [CrossRef]
35. Dai, W.; Yang, J.; Shi, B. Vibration transmission and power flow in impact oscillators with linear and nonlinear constraints. *Int. J. Mech. Sci.* **2020**, *168*, 105234. [CrossRef]
36. Dai, W.; Yang, J. Vibration transmission and energy flow of impact oscillators with nonlinear motion constraints created by diamond-shaped linkage mechanism. *Int. J. Mech. Sci.* **2021**, *194*, 106212. [CrossRef]
37. Yang, J.; Jiang, J.Z.; Neild, S. Dynamic analysis and performance evaluation of nonlinear inerter-based vibration isolators. *Nonlinear Dyn.* **2020**, *99*, 1823–1839. [CrossRef]
38. Nayfeh, A.H.; Mook, D.T. *Nonlinear Oscillations*; Willey: New York, NY, USA, 1979.
39. Abramowitz, M.; Stegun, I.A. *Handbook of Mathematical Functions with Formulas, Graphs, and Mathematical Tables*; Dover Publications: New York, NY, USA, 1972.
40. Press, W.H.; Flannery, B.P.; Teukolsky, S.A.; Vetterling, W.T. *Numerical Recipes: The Art of Scientific Computing*; Cambridge University Press: Cambridge, UK, 1992.
41. Wolf, A.; Swift, J.B.; Swinney, H.L.; Vastano, J.A. Determining Lyapunov exponents from a time series. *Phys. D* **1985**, *16*, 285–317. [CrossRef]
42. Nayfeh, A.H.; Balachandran, B. *Applied Nonlinear Dynamics: Analytical, Computational, and Experimental Methods*; Wiley: New York, NY, USA, 1995.